Exploiting the entire near-infrared spectral range to improve the detection of methane plumes with high-resolution imaging spectrometers

Javier Roger[1], Luis Guanter[1,2], Javier Gorroño[1], and Itziar Irakulis-Loitxate[1,3]

[1]Research Institute of Water and Environmental Engineering (IIAMA), Universitat Politècnica de València (UPV), 46022, Valencia, Spain.
[2]Environmental Defense Fund, Reguliersgracht 79, 1017 LN Amsterdam, The Netherlands.
[3]International Methane Emission Observatory (IMEO), United Nations Environment Programme, Paris, France.

Correspondence: Javier Roger (jarojua@upvnet.upv.es)

Abstract.

Remote sensing has emerged as an important tool for the detection of methane plumes emitted by so-called point sources, which are common in the energy sector (e.g., oil and gas extraction and coal mining activities). In particular, satellite imaging spectroscopy missions covering the shortwave infrared part of the solar spectrum, such as PRISMA, EnMAP or GaoFen-
5 5 AHSI, have proven very effective for this application. These instruments sample the methane absorption features at the spectral regions around 1700 and 2300 nm, which enables the retrieval of per-pixel methane concentration enhancements. Data-driven retrieval methods, in particular those based on the matched filter concept, are widely used to produce maps of methane concentration enhancements from imaging spectroscopy data. These maps are being used for the detection of plumes and the subsequent identification of active sources. However, retrieval artifacts caused by particular surface components may
10 sometimes appear as false plumes or disturbing elements in the methane maps, which complicates the identification of real plumes. In this work, we have used a matched filter that exploits a wide spectral window (1000-2500 nm) instead of the usual 2100-2450 nm window with the aim of reducing the occurrence of retrieval artifacts and background noise. This enables a greater ability to discriminate between surface elements and methane. The improvement in plume detection is evaluated through both simulated data and real data from areas including active point sources, such as the O&G industry from the
15 Permian Basin (U.S.) and the coal mines from the Shanxi region (China). Data sets from the PRISMA, EnMAP, GF5-02 satellite imaging spectrometers missions and from the airborne AVIRIS-NG instrument are used. Results show that the new approach reduces background noise and can remove a great fraction of the retrieval artifacts. For example, the analysis of a scene from the Shanxi region reveals that 15 plumes could be detected from the proposed procedure, whereas only 5 had been identified using the classical matched filter applied to the 2300 nm window. In addition, plume masking derived from this new
20 approach let us propose a new procedure for point source quantification optimized for flux rates values $\leq 1000 \, \mathrm{kg/h}$.

1 Introduction

Since pre-industrial times, the concentration of methane (CH_4) in the atmosphere has increased by more than 150% to a globally-averaged value of 1920 ppb in early 2023 (Dlugokencky, 2023). CH_4 is the second most important greenhouse gas and has been estimated as responsible for almost a third of the warming of the planet so far (Masood et al., 2021). In addition, because of its short lifetime and its a relatively fast mitigation potential (Ocko et al., 2021), reducing atmospheric CH_4 concentration is the most efficient way to curb global warming (Ming et al., 2022).

A great portion of the increase in CH_4 concentration in the atmosphere is due to the growth of anthropogenic emissions from sectors such as agriculture, waste management, coal mining and the oil and gas (O&G) industry. The O&G industry produces approximately 33% of total anthropogenic emissions and has been identified as one of the sectors with the highest potential to reduce emissions (UNEP, 2021), which is also generally considered cost-effective (Mayfield et al., 2017).

An important fraction of the emissions from fossil fuels come from CH_4 point sources (Duren et al., 2019). In this context, satellites have proven to be instrumental in detecting CH_4 plumes originated in this manner. Especially, satellite imaging spectrometers can leverage the CH_4 absorption features in the shortwave infrared (SWIR), where there is a weak ($\sim$1700 nm) and strong ($\sim$2300 nm) absorption window (see Figure 1). Spaceborne measurements of the solar radiation reflected by the Earth's surface can be used to derive CH_4 concentration enhancements from these features.
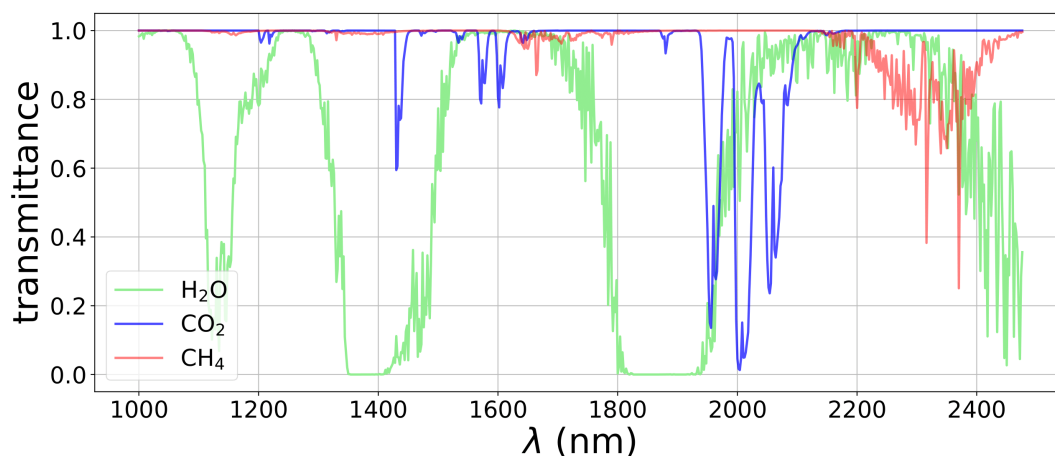
Figure 1. HITRAN derived $transmittance$ spectra of atmospheric H_2O (green), CO_2 (blue), and CH_4 (red) resampled to 2 nm.

Imaging spectrometers, also known as hyperspectral imagers, have a coarse temporal resolution but offer a high spatial and spectral resolution able to resolve a large range of point sources (Irakulis-Loitxate et al., 2021). Of this kind, we find the Italian PRISMA (Precursore IperSpettrale della Missionse Applicativa) mission (Loizzo et al., 2018), the Chinese GF5-02 AHSI (GaoFen-5-02 Advanced HyperSpectral Imagers) mission (Liu et al., 2019), and the German EnMAP (German Environmental Mapping and Analysis Program) mission (Guanter et al., 2015), the three of them with a 30 m spatial resolution and a spectral

resolution ∼10 nm with a spectral coverage of 400-2500 nm. We can also find the constellation of GHGSat, which have a high spatial resolution varying between 25 and 50 m (depending on the satellite). These satellites have built-in Fabry-Pérot spectrometers that operate only in the 1700 nm CH_4 absorption window with a spectral resolution of 0.1 nm (Jervis et al., 2021).

45 In the literature, two types of methodologies have been used to obtain the CH_4 concentration in the scene. First, the so-called physically-based methods, which require an exhaustive knowledge about radiation, its interactions and the media that travels through. And there are also data-driven methods, which statistically derive information from the image itself. The latter type presents lower computational time and partially compensates for radiometric and spectral errors (Thompson et al., 2015; Guanter et al., 2021). Among the possible methods of this class we can find the matched filter.

50 The matched filter applied to the CH_4 case maximizes the score on the pixels that most strongly match the CH_4 absorption spectrum (Manolakis et al., 2007) convolved to the spectral response of the satellite sensor, and the bands selected from the data set are usually those covering the 2300 nm absorption window (2100-2450 nm). Unfortunately, the raw matched filter is prone to disturbing enhancements caused by measurement noise and sensitivity to the surface. Specifically, surface elements with similar absorptive features to CH_4 may lead to systematic errors. These can be abundantly present in heterogeneous scenes and

55 can difficult or mislead the detection of CH_4 plumes. We show an example in Figure 2. The identification of real CH_4 plumes is complicated because of the large number of these disturbing elements across the scene. Therefore, it is necessary to develop new procedures that get to remove them, and consequently, improve the ability to detect CH_4 emissions.

In this work, we have elaborated a matched filter-based retrieval that exploits the whole SWIR spectral region with the aim of improving the detection of CH_4 plumes emitted from point-sources. We implement end-to-end simulations from trace gases to

60 test if atmospheric carbon dioxide (CO_2) and water vapor (H_2O) disturb the CH_4 retrieval when extending the spectral range, and show CH_4 concentration enhancement maps from both simulated and real data that are compared to other state-of-the-art retrieval. Finally, we test the point-source quantification based on a plume masking resulting from this new approach.

2 Materials and Methods

2.1 Matched filter for CH_4 enhancement concentration mapping

65 If radiation arrives at the detector without CH_4 absorption from an emission (L_0) and also with CH_4 absorption (L), according to the Beer-Lambert's law, L will be characterized by

$$L = L_0 e^{\alpha k} \tag{1}$$

where α is the CH_4 concentration enhancement in parts-per-billion (ppb), and k is the CH_4 unit absorption spectrum, which characterizes CH_4 absorption features. Note that the CH_4 concentration enhancement can also be symbolized by ΔXCH_4.

70 k is calculated using a LookUp Table adapted to the angular configuration of the scene and deduced from the HITRAN absorption database (Gordon et al., 2017). Note that HITRAN does not consider scattering, but we can ignore it because it is
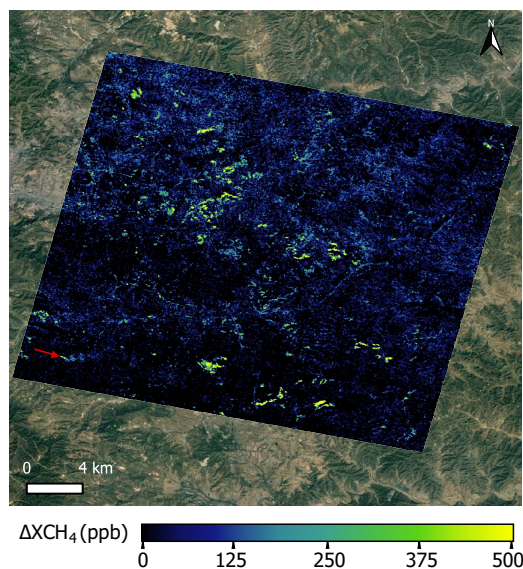
Figure 2. Example of a CH$_4$ concentration enhancement (ΔXCH$_4$) map derived from a PRISMA data set that covers an area of coal mines in the Shanxi region (China). The only detected plume is marked with a red arrow and is originated from a venting shaft. The retrieval is derived from a matched filter formulation using the 2100-2450 nm CH$_4$ absorption window. The true color image source is © Google Earth.

not relevant in the SWIR (Buchwitz et al., 2005). Then, the exponential of the Eq. 1 can be expanded as a Taylor series of infinite terms, and it can be simplified to the second term if we assume a sufficiently small argument of the exponential. This implies that the approximation will generate more accurate results for lower α. Then, assuming this simplification, radiance

75 can be approximated to a linear function of α, which will be used for the matched filter method.

  The matched filter models a scene radiance data cube as a multivariate Gaussian, where each spectral band is considered to follow a Gaussian distribution. The mean vector (μ) and the covariance matrix (Σ) are retrieved from the data cube and characterize the whole image, while assuming enough homogeneity and CH$_4$ emission sparsity through the scene. Then, the radiance spectrum of each pixel (L) can be assessed following two different hypotheses. The null hypothesis (H_0), where radiance is simply assessed as background radiance, and the alternative hypothesis (H_1), where it is assessed as the background

80 radiance plus a term that represents CH$_4$ absorption (Thompson et al., 2016). These hypothesis are represented as follows

$$H_0 : L \sim \mathcal{N}(\mu, \Sigma) \tag{2}$$

$$H_1 : L \sim \mathcal{N}(\mu + \alpha t, \Sigma) \tag{3}$$

85   where $\mathcal{N}$ represents a multivariate Gaussian distribution with the mean vector and covariance matrix located in its first and second arguments, respectively. The CH_4 absorption term from H_1 is given by the linear term αt, that comes from linearizing the exponential function from Eq. 1. t is the target signature that spectrally characterizes the absorption of CH_4 per unit of concentration and is obtained by an element-wise multiplication between the μ and the k arrays, where k is first convolved to the instrument's spectral response. Note that k in satellite-based missions is calculated considering the integration of CH_4 over

90   an 8 km high column such as in Thompson et al. (2016), while in airborne missions is calculated over the specific flight height.

In order to obtain the α values, the probability of H_1 occurring is maximized following the maximum likelihood estimation (Eismann, 2012). As a result, we obtain this expression

$$\alpha = \frac{(L-\mu)^T \Sigma^{-1} t}{t^T \Sigma^{-1} t} \qquad (4)$$

Data sets used in this study come from push-broom imaging spectrometer missions (AVIRIS-NG, GF5-02 AHSI, EnMAP,

95   and PRISMA) that scan the swath of the scene with a 2-D detector array. Differences in central wavelength and spectral resolution can be found among detectors from the same array because of optical aberrations (Guanter et al., 2009), which compromises the uniformity between the data cube columns in the across track direction. Therefore, the matched filter is applied in a per-column basis.

Along the SWIR spectral window there are two CH_4 absorption windows, namely a weaker one around 1700 nm and a

100   stronger one around 2300 nm. The 2300 nm window (roughly 2100-2450 nm) is typically chosen for CH_4 (Thompson et al., 2015; Guanter et al., 2021; Foote et al., 2020; Irakulis-Loitxate et al., 2021) because the more intense absorption allows to better characterize CH_4 in comparison to the other window. Hereinafter we will refer this spectral range selection as 2300-MF. There are usually elements from the scene such as roads, solar panels, and buildings that present absorption features similar to CH_4 in the 2300 nm window. Therefore, we will find retrieval artifacts, i.e., pixels with positive ΔXCH_4 values related to

105   these structures. Retrieval artifacts usually present higher ΔXCH_4 values than background noise and can disturb CH_4 plume detection. In fact, they difficult the identification of the real plumes and can even lead to false positives. In this work, we reduce the presence or the intensity of retrieval artifacts by expanding the matched filter spectral range of application to the whole SWIR (1000 – 2500 nm). Hereinafter we will call this spectral range selection as SWIR-MF. In this spectral range, apart from also accounting for the 1700 nm window, we account for spectral bands with practically no CH_4 absorption. Retrieval artifacts

110   coming from similar features in the 2300 nm window can present other different features along the SWIR where CH_4 does not absorb. This should lead to a greater capability to discriminate between the true CH_4 emissions and retrieval artifacts.

According to Eismann (2012), given a N-dimensional space in which each dimension is referred to each spectral band, the matched filter direction is determined through a balance between the minimum background variance direction and the reference spectrum direction ($\boldsymbol{\mu} + \alpha \, \mathbf{t}$). The matched filter direction defines the regions in the N-dimensional space where CH_4 emission

115   related pixels should be found. We can observe this in the top panel from Figure 3, where an scatter plot from a matched filter that used only 2 bands from a EnMAP data set from a site in an O&G field in Turkmenistan is illustrated. One band is located at 2191 nm, where there is barely CH_4 absorption, while the other one shows a prominent absorption in 2369 nm. We can

observe that values that more strictly follow the matched filter direction have greater α values, which are generally related to CH_4 emission pixels. When opening the spectral window to the whole SWIR spectrum the reference spectrum to match is

120 more demanding, which would attenuate or remove retrieval artifacts because spectral features beyond the 2300 nm window penalize them.
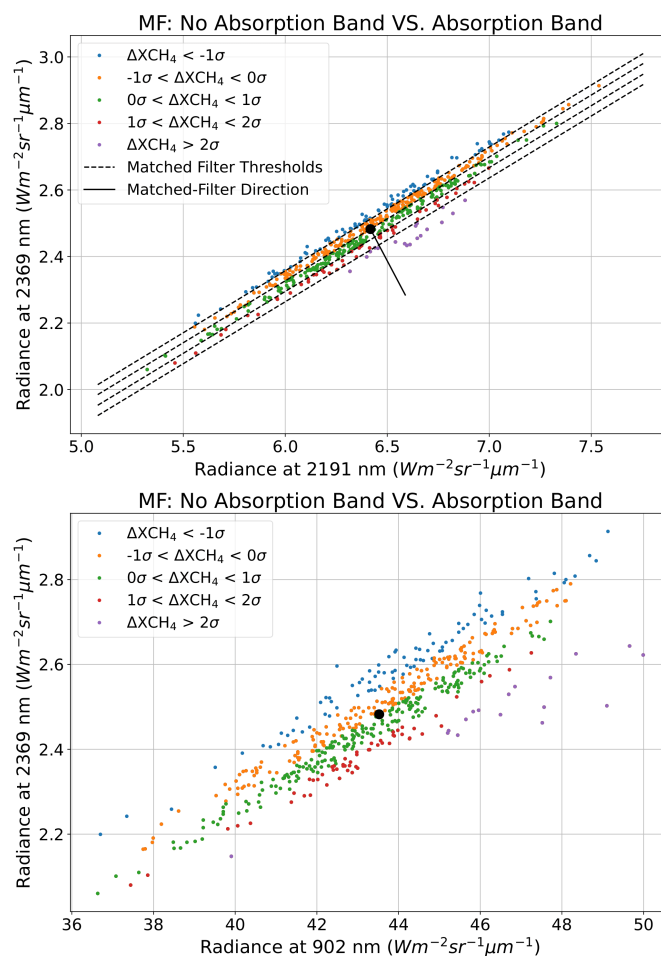
Figure 3. Scatter plots showing the comparison between the 2191 nm (top)/ 902 nm (bottom) no absorption bands and the 2369 nm absorption band. Data points are colored according to where they are located in the Gaussian distribution based on the matched filter retrieval derived from an EnMAP data set showing an O&G field located in Turkmenistan with CH_4 emissions. The top panel also shows the matched filter threshold lines and the matched filter direction.

Although SWIR-MF reduces retrieval artifacts with respect to 2300-MF, there are some limitations when using it. New retrieval artifacts can appear because we are including the 1700 nm absorption window. However, they are attenuated in the same manner as those from the 2300 nm window. In addition, due to the use of a wide spectral window, another limitation

125   comes from including spectrally distant bands, which present a higher degree of decorrelation. We can see this in the bottom

panel from Figure 3, where we find a similar scatter plot to the one at the top panel but changing the no absorption band to

another one that is spectrally more distant at 902 nm. In comparison to the previous scatter plot, we can observe that data

points are more scattered than in the first plot. Additionally, in Figure 4 a correlation matrix from this data set is illustrated and

shows us that distant bands (upper-right and lower-left corners) have lower correlation, which leads to a lower weight of the

130   background variance direction. This difficults the discrimination between plume pixels and background pixels, which can lead

to enhanced background clutter and plume pixel attenuation. Note that there are bands with very low correlation because of the

strong H_2O and CO_2 absorption. We remove these bands from the SWIR-MF in order to not account for their negative impact.
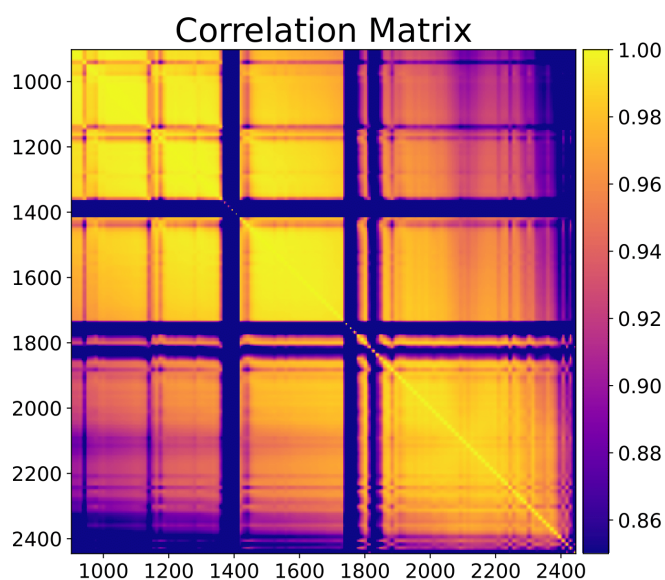
Figure 4. Correlation matrix of the SWIR spectral bands from a data set showing an O&G field located in Turkmenistan with CH_4 emissions. Note that the axes reflect the wavelength values in nm of the spectral bands.

We have not considered yet interferences with other traces gases such as the H_2O and CO_2 on the not removed bands (see

Figure 1). Absorption features from these gases appear along the SWIR spectral region and might disturb CH_4 retrieval values.

135   Generally, H_2O and CO_2 atmospheric concentrations are approximately homogeneous across the area captured in one data set.

However, atmospheric concentration variations of H_2O are given when there are pronounced height variations of the terrain

across the scene (Lou et al., 2021). Thus, unless the data set area meets this condition, we can assume homogeneity. As a result,

variations from the mean array could not be related to these gases, which implies that the matched filter should not be affected

by them. Nevertheless, there are cases of coemission of CH_4 and CO_2 plumes such as in inefficient flaring (Irakulis-Loitxate

140   et al., 2021). In these cases, the CO_2 presence would disturb the CH_4 detection because the radiance spectra from these pixels

would be deviated from the reference spectrum, which should result in a lower enhancement.

Then, with SWIR-MF we will obtain greater enhancement values coming from 1700 nm retrieval artifacts and clutter, while there will be lower enhancement from 2300 nm retrieval artifacts and plume pixels. Even lower enhancements will be found in the case of CO_2 and CH_4 plume overlapping. Therefore, SWIR-MF values greater than the 2300-MF values come from disturbing factors. Most of the pixels meeting this condition belonged to the negative part of the normal distribution of the 2300-MF values because they were not considered as CH_4 in this spectral window, but with SWIR-MF they are converted into positive due to 1700 nm retrieval artifacts and the emergence of new clutter noise. As a solution, we change these values to the ones of the original 2300-MF in order to penalize the increased enhancement. This generates a greater contrast between the emission and its surroundings because a great fraction of the transformed values present negative values. On the other hand, to solve the underestimation from plume pixels and make values comparable to the 2300-MF values, we multiply the remaining retrieval values by a factor f defined as

$$f = \frac{\sigma_{\text{2300-MF}}}{\sigma_{\text{SWIR-MF}}} \tag{5}$$

where $\sigma_{\text{2300-MF}}$ and $\sigma_{\text{SWIR-MF}}$ are the standard deviations from the retrievals resulting from applying the 2300-MF and the SWIR-MF, respectively. Retrievals follow a normal distribution with an averaged value of ~ 0, so we can scale the distribution of not-transformed SWIR-MF values to the one of the the 2300-MF values by simply multiplying by f. Then, the transformed values from the SWIR-MF retrieval will follow approximately the 2300-MF retrieval normal distribution. In this manner, plume pixel values will be approximately scaled to the enhancement levels from the 2300-MF retrieval in order to solve the underestimation. Note that we will call this procedure as Combo-MF and a flow chart depicting how it is obtained is illustrated in Figure 5. As a result, limitations from the SWIR-MF are mitigated: disturbing 1700 nm retrieval artifacts and new clutter noise are removed, and the SWIR-MF values are transformed into typical 2300-MF value levels. In Figure 6 we can see retrieval histograms from a EnMAP data set from an O&G field in Turkmenistan when applying 2300-MF, SWIR-MF, and Combo-MF. We can observe that SWIR-MF has a lower standard deviation because of a more stringent spectrum that penalizes retrieval artifacts and underestimates plume ΔXCH_4. The Combo-MF takes a standard deviation close to the one from the 2300-MF because of the scaled values, but its mean is shifted to negative values because a great fraction of the 2300-MF values from Combo-MF are negative. Therefore, there is a lower amount of pixels with positive enhancent, which implies a better contrast between plume pixels and their background. Note that pixels with overlapped CO_2 and CH_4 plumes would still suffer from underestimation, which can be relevant depending on how concentrated is the CO_2 plume.

Combo-MF is not the unique alternative created to improve CH_4 emission detection. Instead, there exist other matched filter derived methods such as the *Matched filter with Albedo correction and reweighted L1 sparsity code* (MAG1C) that has been used in some studies (Foote et al., 2021; Knapp et al., 2023; Ayasse et al., 2022). It applies an albedo correction across the radiance data cube in order to account for the homogeneity assumption from the matched filter. In addition, MAG1C leverages the CH_4 sparsity assumption and also applies an iterative regularization that aims to reduce background noise. MAG1C retrievals values can be divided in two groups: 1) zero-values that were obtained because of the sparsity assumption and 2) a set of values that follow a log-normal distribution and mostly refer to retrieval artifacts and CH_4 emissions. If we
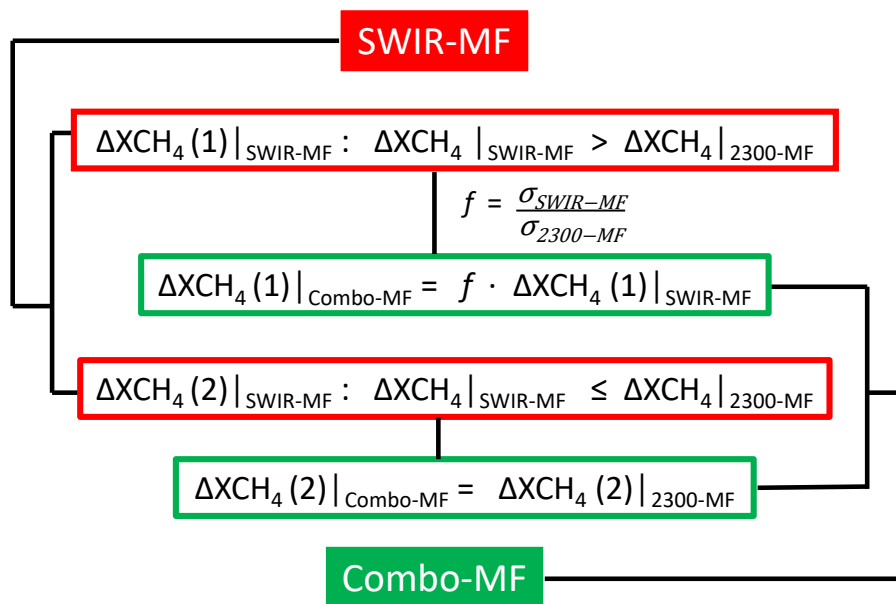
Figure 5. Diagram describing how Combo-MF is carried out from the SWIR-MF and 2300-MF values.
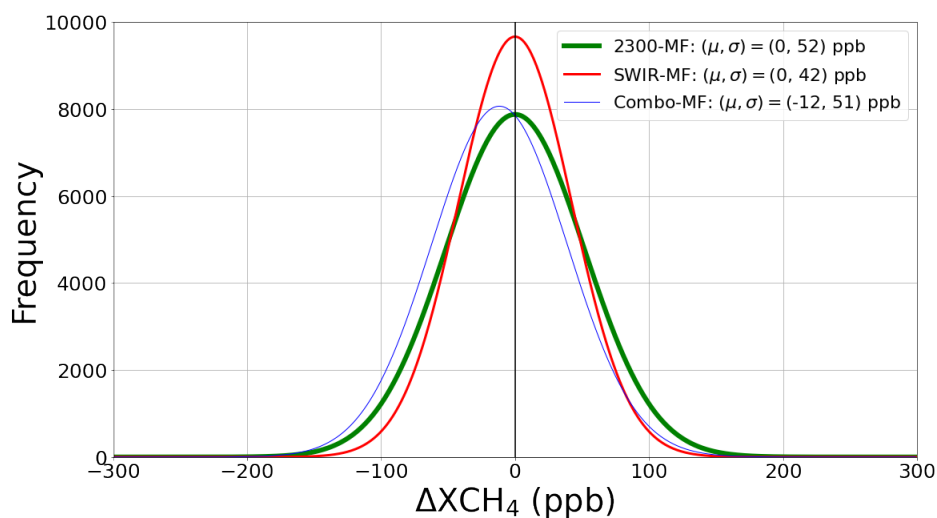
Figure 6. Histrogram from 2300-MF (green), SWIR-MF (red), and Combo-MF (blue) retrieval histograms from an EnMAP data set showing a O&G field located in Turkmenistan with CH_4 emissions. μ and σ are the mean and standard deviation values from the different distributions, respectively.

175 transform the retrieval in order to follow a normal distribution, the resulting standard deviation will not be related to the random background noise, as happens with Combo-MF, and therefore we will not be able to compensate a potential underestimation when extending the spectral window. Because of this reason, we will not apply an equivalent Combo-MF methodology to MAG1C. Thus, we will compare MAG1C retrievals using the 2300 nm absorption window (2300-MAG1C) and the whole SWIR spectral region (SWIR-MAG1C) to the Combo-MF retrievals in order to assess if the latter improves plume detection.

2.2 Simulated trace gas enhancements

ΔXCH_4 maps depicting simulated plumes with different shapes, related wind speed values, and concentrations have been generated using large-eddy simulations with the Weather and Research Forecasting Model (WRF-LES) (Varon et al., 2018; Cusworth et al., 2019). These plumes are implemented in three different data sets from the PRISMA mission to assess the CH_4 emission detection and quantification capabilities from the different procedures.

185 In addition, simulated enhancements from H_2O and CO_2 have been implemented homogeneously across the whole area extent from a PRISMA data set. Specifically, typical background enhancements of 2500–10000 ppb for CO_2 (C3S, 2018) and of 1–2.5 g/cm^2 for H_2O (Mieruch et al., 2014) were implemented homogeneously across this data set in order to study how atmospheric concentrations of these trace gases would affect CH_4 retrievals when using 2300-MF and SWIR-MF. In this manner, we can test whether a greater or lower background concentrations of these two trace gases have an impact in CH_4

190 retrieval. However, because of the homogeneity of these enhancements across the scene there should not be any deviation from the mean value that could be related to them. Therefore, this enhancements should not disturb retrieval values.

2.3 Quantification of point-source emissions

The parameter typically used to quantify the intensity of a CH_4 emission released from a point-source is the flux rate (Q in kg/h). As in Varon et al. (2018), we can express this magnitude as

$$Q = \frac{U_{\text{eff}} \cdot \text{IME}}{L} \tag{6}$$

where U_{eff} (m/s) is the effective wind speed, a parameter that linearly depends on the wind speed at 10 m above the surface (U_{10}) that is given as an output from the WRF-LES simulations, L (m) is obtained as the square root of the plume mask area, and IME (kg) is the mass related to the enhancement contained in the masked plume (Frankenberg et al., 2016). IME and L depend on the plume mask, which makes masking an important factor that impacts on the accuracy of quantification. Masking

200 is done by the following steps:

1) A median filter is applied to the retrieval to remove high-frequency variations related to background noise.

2) We create a mask that only filters those values from the resulting median filter retrieval that are greater than 1 standard deviation from the retrieval. We use 1 standard deviation because it is the value at which we consider that we can detect

Table 1. Mission, location, sector where the CH_4 emission was originated, date, and central coordinates from the data sets used in this study. Dates are in YYYY-MM-DD format, and latitude and longitude coordinates (*Lat/Lon*) are in decimal degrees.

Mission	Location	Sector	Date	Lat/Lon
EnMAP	Ekizak (Turkmenistan)	O&G	2022-10-02	38.685/54.243
PRISMA	Silesia (Poland)	Coal mining	2022-03-02	50.110/17.895
PRISMA	In Amenas (Algeria)	O&G	2021-01-15	28.286/9.638
PRISMA	Permian Basin (U.S.)	O&G	2020-06-30	31.437/-103.480
GF5-02 AHSI	Permian Basin (U.S.)	O&G	2022-02-09	32.798/-104.124
AVIRIS NG	San Joaquin Valley (U.S.)	O&G	2017-09-06	35.279/-119.476
EnMAP	Delhi (India)	Landfills	2023-04-24	28.620/77.200
PRISMA	Shanxi (China)	Coal mining	2021-02-06	36.241/112.909

the plume by visual inspection (Guanter et al., 2021). Note that for the Combo-MF we use the standard deviation of the
205   2300-MF retrieval because its values are scaled to 2300-MF values.

3) We select the overlapped pixels from two masks. One is the resulting mask from the previous step and the other one delimits the plume shape coming directly from the simulation. This is done because we only want to keep those pixels related to the plume area.

Combo-MF retrievals present a lower background noise at positive values, which makes it easier to isolate the plume from
210   its sorroundings. This should positively affect masking, although values transformed by a simple factor in the Combo-MF retrieval should not be trusted for quantification. Thus, we will compare the quantification based exclusively on the 2300-MF and, the quantification based on 2300-MF values and Combo-MF masking. This quantification strategy that mix both retrievals will be called Mix-MF.

2.4   Imaging spectroscopy data

215   In this work we have used Top-of-Atmosphere radiance data sets from the PRISMA, GF5-02 AHSI, EnMAP and AVIRIS-NG missions. In order to implement simulated trace gases enhancements we have chosen PRISMA samples from a desertic O&G field in Argelia, an O&G field from the Permian Basin (U.S.), and a coal mine site in Poland (see Figure 7. Additionally, we show retrievals with detected CH_4 plumes also derived from PRISMA samples from coal mines in the Shanxi region (China)

(Figure 12). We also present a GF5-02 AHSI sample with overlapped CH_4 and CO_2 plumes from the Permian Basin (U.S.)
coming from an inefficient flare (Figure 9). Moreover, an EnMAP sample from an O&G field in Turkmenistan is chosen to
study the matched filter using only two bands, the decorrelation between all the SWIR bands, and to obtain the histograms
(shown in Figure 6) resulting from applying different procedures. From this mission, we also show the retrievals from a data
set capturing a Delhi (India) area where there are the Bhalswa, Gazhipur and Okhla landfills (Figure 11). Finally, an AVIRIS-
NG sample from an O&G field in San Joaquin Valley in California (U.S.) is used in order to show the performance of 2300-MF,
Combo-MF, 2300-MAG1C and SWIR-MAG1C procedures (Figure 10). More information about these data sets can be found
in Table 1.

3 Results

3.1 Real data with simulated trace gas enhancements
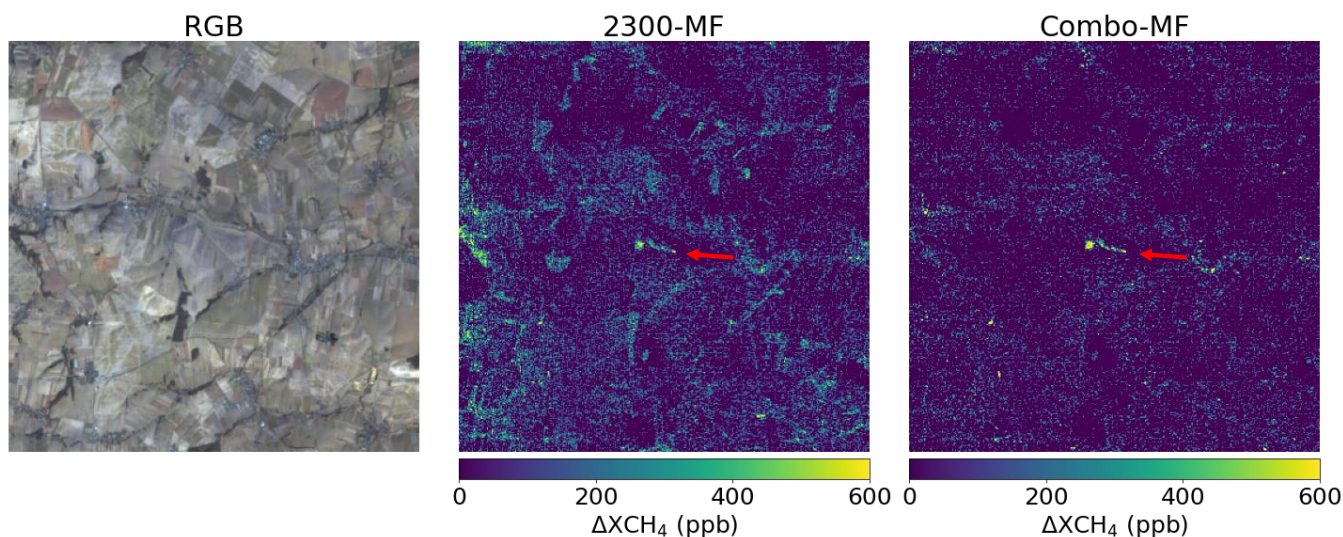
Figure 7. True color image (left), 2300-MF retrieval (center), and Combo-MF retrieval (right) from a PRISMA data set from a coal mine site
in Poland with an implemented plume with $Q = 2000 \, \mathrm{kg/h}$. The plume is pointed with an arrow.

We have implemented simulated CH_4 plumes in three PRISMA data sets from three different sites. These areas were selected
to study a diverse range of scenarios regarding surface heterogeneity and brightness, which are important factors in the matched
filter retrieval. Homogeneous and bright surfaces would lead to a better performance than more heterogeneous and darker
surfaces. The areas selected were an homogeneous and bright desertic O&G site from Algeria, an heterogenous and bright
O&G site from the Permian Basin (U.S.), and an heterogeneous and relatively dark coal mining site in Poland.
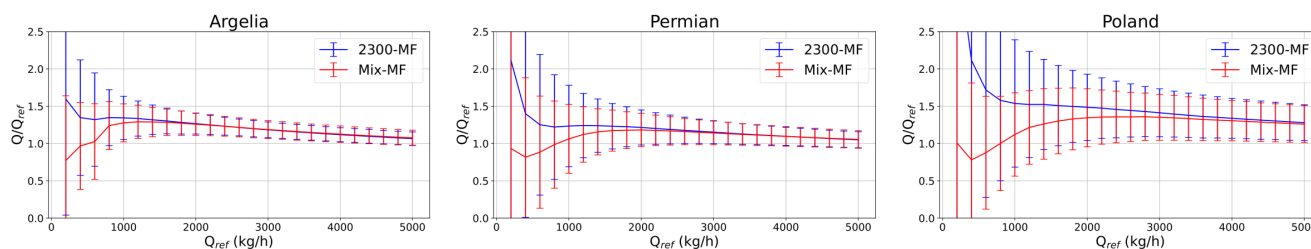
Figure 8. Simulated flux rate Q_{ref} versus the ratio between the deduced flux rate Q and Q_{ref} from 100 different plumes implemented in PRISMA data sets from sites in Argelia (top), the Permian Basin (center), and Poland (bottom). Plotted points and error bars of each flux rate value correspond to the mean and 1 standard deviation values from the 100 estimates, respectively.

In Figure 7 we show an RGB image and 2300-MF and Combo-MF retrievals from the Poland site. We can observe a
235   remarkable reduction in the positive background noise values and the attenuation of retrieval artifacts related to the scene topography or to different land covers. As a result, there is a greater contrast between the plume and its surroundings and therefore it is easier to detect the emission by visual inspection. On the other hand, Figure 8 shows the quantification based entirely on the 2300-MF retrieval and the Mix-MF quantification. They are applied in data sets capturing Argelia, Permian Basin, and Poland sites. The study was made for a flux rate interval ranging from $200\,\text{kg/h}$ to $5000\,\text{kg/h}$ for 5 different plumes
240   with different shape and ΔXCH_4 distribution. Each one of these plumes was implemented 20 times across each data set in different locations for each flux rate value, i.e., quantification was assessed with 100 plumes for each flux rate value. In this manner, we make the study considering plume and background diversity within the same data set. Error bars showing 1 standard deviation from the 100 plume quantification distribution for each flux rate value are displayed. We find that Argelia and Permian Basin sites present lower uncertainty than the Poland site because the lower brightness from the latter is translated in a lower
245   retrieved signal-to-noise-ratio. For $Q < 1000\,\text{kg/h}$, the low ΔXCH_4 plume values, closer to noise level, difficult the masking process. In the 2300-MF quantification case we find an overestimation, while for the Mix-MF quantification we find that the more restrictive masking leads to more accurate values. However, for both procedures there is an important uncertainty at these flux rate levels that limits quantification. For greater Q, there is a progressive uncertainty and overestimation reduction for both procedures that approximates quantification to true values. At these levels, estimations from both quantification strategies align
250   because the greater enhancement from plume pixels lead to a practically identical masking for both of them.

In addition, typical background enhancements of CO_2 and H_2O were implemented homogeneously across these three data sets in order to assess their impact in 2300-MF and SWIR-MF retrievals. As a result, we found practically null differences between the enhanced and not enhanced data sets using both procedures. Therefore, atmospheric concentrations of these trace do not disturb the retrievals. On the other hand, we have also studied the influence of CO_2 plumes overlapping CH_4 plumes in
255   the retrieval when using CO_2 absorption bands. This overlap can be originated from inefficient flares in O&G fields (Irakulis-Loitxate et al., 2021). One example of this from a GF5-02 AHSI data set is illustrated in Figure 9. At the left panel, we can observe a white dot in the 2016 nm radiance band associated to the flare. Comparing the 2300-MF (center) and Combo-
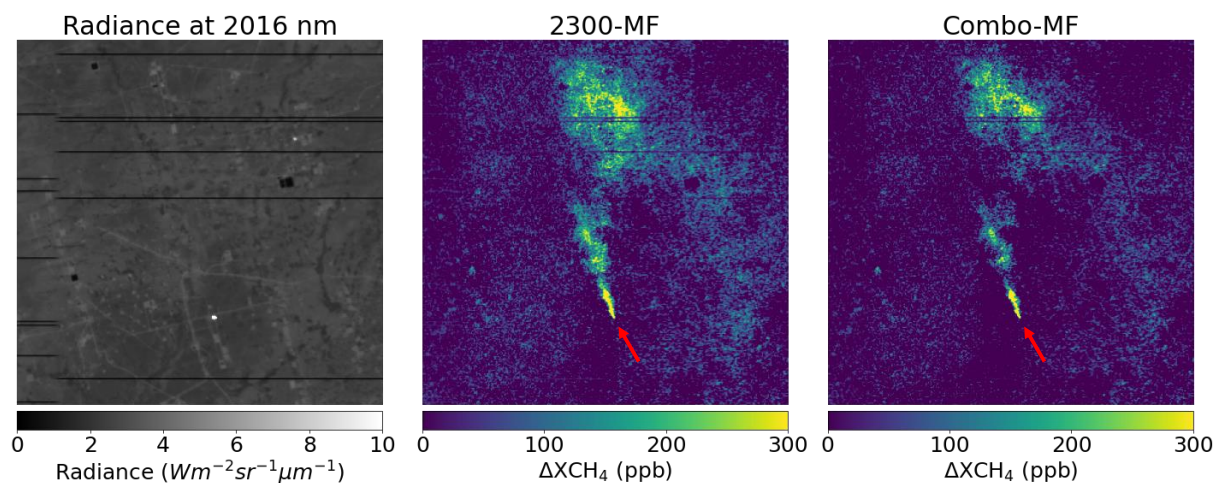
Figure 9. Radiance at 2016 nm (left), 2300-MF retrieval (center), and Combo-MF retrieval (right) from a GF5-02 AHSI data set from an O&G field in the Permian Basin (U.S.) showing a plume (pointed with an arrow) originated from inefficient flaring.

MF (right) retrievals, we can see that background noise from the latter is reduced, but there is also an attenuation of plume pixel enhancements. Therefore, we can deduce that coexistence with CO_2 plumes might derive in an underestimation of CH_4 plume enhancement. Greater underestimation would occur when coemitting with more concentrated CO_2 plumes since the approximation to the reference spectrum would be less accurate.

3.2 Real CH_4 plume cases

3.2.1 Comparison to MAG1C retrievals with AVIRIS-NG data

In Figure 10, we compare ΔXCH_4 retrievals using 2300-MF, Combo-MF, 2300-MAG1C, and SWIR-MAG1C from an O&G field site in San Joaquin Valley (U.S.). We evaluate the performance when widening the spectral window to the whole SWIR spectrum, and assess if there is an improvement in comparison to the Combo-MF performance. The upper limit value selected for representation was different for 2300-MF and Combo-MF retrievals than for 2300-MAG1C and SWIR-MAG1C retrievals. As shown in Guanter et al. (2021), we can find that MAG1C exhibits higher values and therefore a higher upper limit was set to compare retrievals showing approximately the same plume intensity. Therefore, we will be able to assess the contrast between plumes (pointed with arrows) and their surroundings for the different retrievals. 2300-MAG1C retrieval presents a higher number of retrieval artifacts than 2300-MF. These are further attenuated or totally removed in the SWIR-MAG1C retrieval. However, SWIR-MAG1C enhances some retrieval artifacts that are not shown when using Combo-MF. The latter leads to a lower background noise in comparison to 2300-MF, although it is slightly higher in comparison to MAG1C retrievals because they use the sparstiy assumption. Therefore, Combo-MF can be considered as an effective trade-off between reducing

275 background noise and retrieval artifacts. Note that instead of considering a 8 km high column for CH_4 integration, we have used the scene average sensor altitude obtained from the metadata (2.48 km).
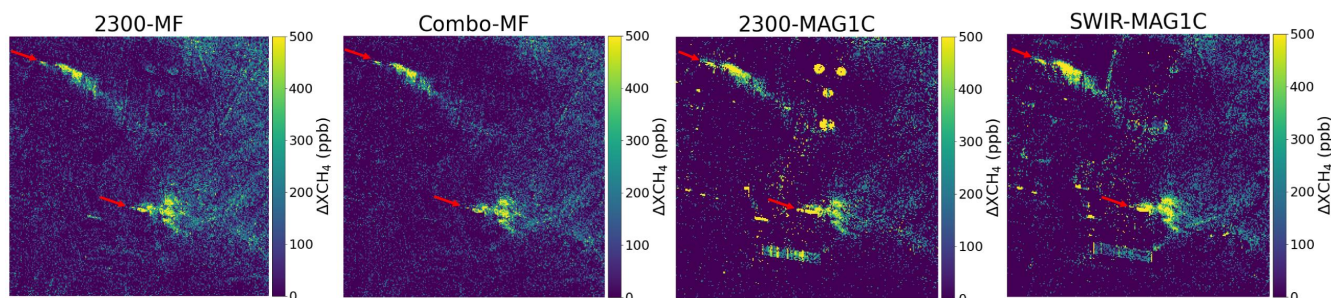
Figure 10. Starting from the left, 2300-MF, Combo-MF, 2300-MAG1C, and SWIR-MAG1C retrievals from an AVIRIS-NG data set showing an O&G field in San Joaquin Valley, California (U.S.). The first two and the last two retrievals were illustrated with a different range of values in order to compare them by visual inspection. Plumes are pointed with an arrow.

3.2.2 Retrieval performance in a landfill area using EnMAP data

Landfill emissions can be detected using EnMAP data (Roger et al., 2023), so we look for some examples using data sets capturing areas with landfills. In Figure 11 we can observe the comparison between the 2300-MF and Combo-MF retrievals

280 from an EnMAP data set from a Delhi area (India). Here there are located the Bhalswa (top-left), Gazhipur (top-right) and Okhla (bottom) landfills. We can observe the enhancement related to these three landfills (pointed with an arrow) in both retrievals. However, the 2300-MF shows a great amount of retrieval artifacts related to the urban area and a higher background noise, while the Combo-MF further attenuates or removes these retrieval artifacts and reduces the positives values from background noise. We can see that the enhancement from the landfills is somewhat attenuated in the Combo-MF, which migh be caused because

285 of the existence of retrieval artifacts below the emission. Even though, the capability for emission detection is remarkably improved.

3.2.3 Retrieval performance in a coal mining site using PRISMA data

Combo-MF is well-suited for regions with pronounced heterogeneity because there are usually more retrieval artifacts that can be removed. In order to demonstrate this, we do a comprehensive study in a PRISMA data set from a coal mining site in

290 Shanxi (China), which can be considered heterogeneous. First, we identify by visual inspection the CH_4 emissions with the 2300-MF retrieval and then we do the same based on the Combo-MF retrieval. In Figure 12 we can observe both retrievals with arrows pointing to the identified plumes of each retrieval, which mainly are originated from venting shafts. There is a lower background noise and a lower number of retrieval artifacts when using Combo-MF. This helped to determine whether potential plumes that remained doubtful with 2300-MF were actually true plumes. As a result, while only 5 plumes were identified with

295 2300-MF, 15 plumes were detected with Combo-MF.
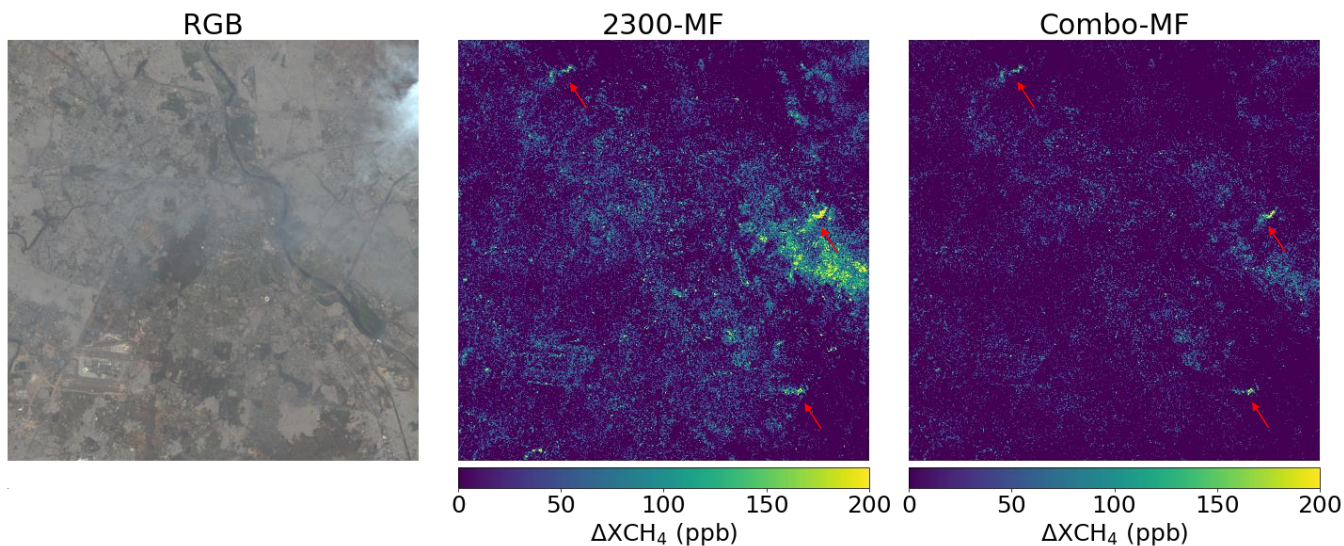
Figure 11. True color image (left), 2300-MF retrieval (center), and Combo-MF retrieval (right) from an EnMAP data set from Delhi (India) showing the Bhalswa (top-left), Gazhipur (top-right) and Okhla (bottom) landfill emissions (pointed with an arrow).
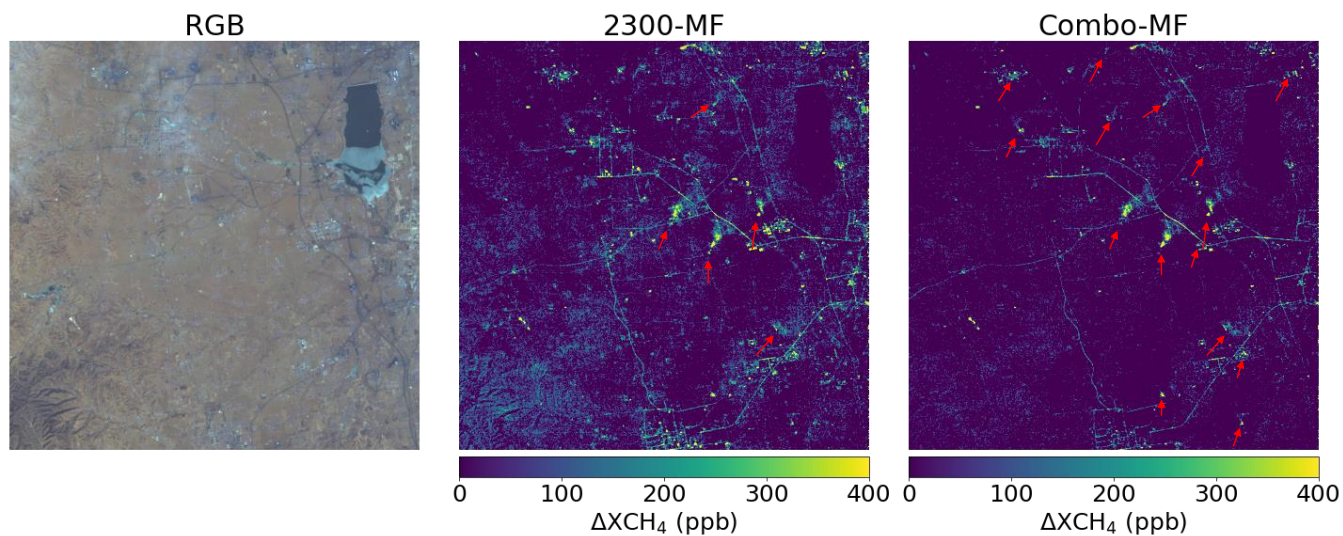
Figure 12. True color image (left), 2300-MF retrieval (center), and Combo-MF retrieval (right) from a PRISMA data set from a coal mine site in Shanxi (China) showing the detected plumes (marked with arrows) with each procedure.

4 Summary and conclusions

In this work, we propose a new matched filter-based retrieval that attenuates or removes retrieval artifacts and also reduces the positive values of background noise, which leads to a greater capability for CH_4 emission detection. First, simulated plumes have been implemented in different data sets and a visual comparison has been made. Second, we have done a quantification assessment using different masking methods. Third, the disturbance of H_2O and CO_2 in CH_4 retrievals has also been assessed by means of simulations and analysis of real cases. Finally, retrievals containing CH_4 plumes from real AVIRIS-NG, GF5-02 AHSI, and PRISMA data sets have been assessed in order to compare the proposed procedure to already existing procedures by visual inspection.

Comparing Combo-MF to the common 2300-MF through simulated and not-simulated data sets from different missions, we find that Combo-MF reduces the positive background noise values and attenuates or even practically removes retrieval artifacts coming from topography or other structures, while keeping ΔXCH_4 levels from plumes. However, the interference of CO_2 plumes with CH_4 emissions such as in inefficient flaring can lead to an attenuation of the plume enhancement in the ΔXCH_4 maps. Regarding atmospheric H_2O and CO_2 concentrations, there is practically no disturbance in the retrievals because of the homogeneity of these trace gases across the scenes. We have also tested MAG1C with the 1000-2500 nm spectral range and have found that there is a reduction of retrieval artifacts in comparison to the default 2122-2488 nm window. MAG1C retrievals present a lower background noise, but also plumes with higher score and a greater number of disturbing retrieval artifacts in comparison to Combo-MF retrievals. Therefore, Combo-MF can be considered as an optimal trade-off between background noise reduction and retrieval artifact attenuation, which leads to a better plume detection capability. This is illustrated by a comprehensive analysis in a PRISMA data set from a coal mine site in China found 5 plumes using 2300-MF, but 15 when using Combo-MF. In addition, flux rate estimations from simulated plumes ranging from 200 to 5000 kg/h revealed that plume masking derived from Combo-MF could result in more accurate values than those derived from 2300-MF.

Data availability. Data will be made available on request.

Author contributions. **Javier Roger**: Conceptualization, Methodology, Formal analysis, Investigation, Writing – original draft, Writing – review & editing. **Luis Guanter**: Conceptualization, Resources, Writing – review & editing, Supervision. **Javier Gorroño**: Conceptualization, Methodology, Writing – review & editing. **Itziar Irakulis-Loitxate**: Formal Analysis, Resources, Writing – review & editing.

Competing interests. The authors declare that they have no conflict of interest.

Acknowledgements. The authors thank the Italian Space Agency, the DLR Space Agency, the GaoFen team and, JPL team for the PRISMA, EnMAP, GaoFen-5, GaoFen-5-02, and AVIRIS-NG data used in this work, respectively. We are grateful to Daniel J. Varon for the WRF-LES modelled plumes used in this study. Authors Javier Roger, Javier Gorroño, and Luis Guanter received funding from ESA contract 4000134929.

References

Ayasse, A. K., Thorpe, A. K., Cusworth, D. H., Kort, E. A., Negron, A. G., Heckler, J., Asner, G., and Duren, R. M.: Methane remote sensing and emission quantification of offshore shallow water oil and gas platforms in the Gulf of Mexico, Environmental Research Letters, 17, 084 039, https://doi.org/10.1088/1748-9326/ac8566, 2022.

330   Buchwitz, M., de Beek, R., Noël, S., Burrows, J. P., Bovensmann, H., Bremer, H., Bergamaschi, P., Körner, S., and Heimann, M.: Carbon monoxide, methane and carbon dioxide columns retrieved from SCIAMACHY by WFM-DOAS: year 2003 initial data set, Atmospheric Chemistry and Physics, 5, 3313–3329, https://doi.org/10.5194/acp-5-3313-2005, 2005.

C3S, C. D. S.: Carbon dioxide data from 2002 to present derived from satellite observations. Copernicus Climate Change Service (C3S) Climate Data Store (CDS), accessed: 31-05-2023), 10.24381/cds.f74805c87, 2018.

335   Cusworth, D. H., Jacob, D. J., Varon, D. J., Chan Miller, C., Liu, X., Chance, K., Thorpe, A. K., Duren, R. M., Miller, C. E., Thompson, D. R., Frankenberg, C., Guanter, L., and Randles, C. A.: Potential of next-generation imaging spectrometers to detect and quantify methane point sources from space, Atmospheric Measurement Techniques, 12, 5655–5668, https://doi.org/10.5194/amt-12-5655-2019, 2019.

Dlugokencky, E.: https://gml.noaa.gov/ccgg/trends_ch4/, accessed: 2023-06-06, 2023.

Duren, R., Thorpe, A., Foster, K., Rafiq, T., Hopkins, F., Yadav, V., Bue, B., Thompson, D., Conley, S., Colombi, N., Frankenberg, C.,
340   McCubbin, I., Eastwood, M., Falk, M., Herner, J., Croes, B., Green, R., and Miller, C.: California's methane super-emitters, Nature, 575, 180–184, https://doi.org/10.1038/s41586-019-1720-3, 2019.

Eismann, M.: Hyperspectral Remote Sensing, vol. PM210 of *SPIE Press Monograph*, Society of Photo Optical, 2012.

Foote, M. D., Dennison, P. E., Thorpe, A. K., Thompson, D. R., Jongaramrungruang, S., Frankenberg, C., and Joshi, S. C.: Fast and Accurate Retrieval of Methane Concentration From Imaging Spectrometer Data Using Sparsity Prior, IEEE Transactions on Geoscience and Remote
345   Sensing, 58, 6480–6492, 2020.

Foote, M. D., Dennison, P. E., Sullivan, P. R., O'Neill, K. B., Thorpe, A. K., Thompson, D. R., Cusworth, D. H., Duren, R., and Joshi, S. C.: Impact of scene-specific enhancement spectra on matched filter greenhouse gas retrievals from imaging spectroscopy, Remote Sensing of Environment, 264, 112 574, https://doi.org/https://doi.org/10.1016/j.rse.2021.112574, 2021.

Frankenberg, C., Thorpe, A. K., Thompson, D. R., Hulley, G., Kort, E. A., Vance, N., Borchardt, J., Krings, T., Gerilowski, K.,
350   Sweeney, C., Conley, S., Bue, B. D., Aubrey, A. D., Hook, S., and Green, R. O.: Airborne methane remote measurements reveal heavy-tail flux distribution in Four Corners region, Proceedings of the National Academy of Sciences, 113, 9734–9739, https://doi.org/10.1073/pnas.1605617113, 2016.

Gordon, I., Rothman, L., Hill, C., Kochanov, R., Tan, Y., Bernath, P., Birk, M., Boudon, V., Campargue, A., Chance, K., Drouin, B., Flaud, J.-M., Gamache, R., Hodges, J., Jacquemart, D., Perevalov, V., Perrin, A., Shine, K., Smith, M.-A., Tennyson, J., Toon, G., Tran, H.,
355   Tyuterev, V., Barbe, A., Császár, A., Devi, V., Furtenbacher, T., Harrison, J., Hartmann, J.-M., Jolly, A., Johnson, T., Karman, T., Kleiner, I., Kyuberis, A., Loos, J., Lyulin, O., Massie, S., Mikhailenko, S., Moazzen-Ahmadi, N., Müller, H., Naumenko, O., Nikitin, A., Polyansky, O., Rey, M., Rotger, M., Sharpe, S., Sung, K., Starikova, E., Tashkun, S., Auwera, J. V., Wagner, G., Wilzewski, J., Wcisło, P., Yu, S., and Zak, E.: The HITRAN2016 molecular spectroscopic database, Journal of Quantitative Spectroscopy and Radiative Transfer, 203, 3–69, https://doi.org/https://doi.org/10.1016/j.jqsrt.2017.06.038, hITRAN2016 Special Issue, 2017.

360   Guanter, L., Segl, K., Sang, B., Alonso, L., Kaufmann, H., and Moreno, J.: Scene-based spectral calibration assessment of high spectral resolution imaging spectrometers, Opt. Express, 17, 11 594–11 606, https://doi.org/10.1364/OE.17.011594, 2009.

Guanter, L., Kaufmann, H., Segl, K., Foerster, S., Rogass, C., Chabrillat, S., Kuester, T., Hollstein, A., Rossner, G., Chlebek, C., and et al.: The EnMAP Spaceborne Imaging Spectroscopy Mission for Earth Observation, Remote Sensing, 7, 8830–8857, https://doi.org/10.3390/rs70708830, 2015.

365 Guanter, L., Irakulis-Loitxate, I., Gorroño, J., Sánchez-García, E., Cusworth, D. H., Varon, D. J., Cogliati, S., and Colombo, R.: Mapping methane point emissions with the PRISMA spaceborne imaging spectrometer, Remote Sensing of Environment, 265, 112 671, https://doi.org/https://doi.org/10.1016/j.rse.2021.112671, 2021.

Irakulis-Loitxate, I., Guanter, L., Liu, Y.-N., Varon, D. J., Maasakkers, J. D., Zhang, Y., Chulakadabba, A., Wofsy, S. C., Thorpe, A. K., Duren, R. M., Frankenberg, C., Lyon, D. R., Hmiel, B., Cusworth, D. H., Zhang, Y., Segl, K., Gorroño, J., Sánchez-García, E., Sulprizio,

370 M. P., Cao, K., Zhu, H., Liang, J., Li, X., Aben, I., and Jacob, D. J.: Satellite-based survey of extreme methane emissions in the Permian basin, Science Advances, 7, https://doi.org/10.1126/sciadv.abf4507, 2021.

Jervis, D., McKeever, J., Durak, B. O. A., Sloan, J. J., Gains, D., Varon, D. J., Ramier, A., Strupler, M., and Tarrant, E.: The GHGSat-D imaging spectrometer, Atmospheric Measurement Techniques, 14, 2127–2140, https://doi.org/10.5194/amt-14-2127-2021, 2021.

Knapp, M., Scheidweiler, L., Külheim, F., Kleinschek, R., Necki, J., Jagoda, P., and Butz, A.: Spectrometric imaging of sub-hourly methane

375 emission dynamics from coal mine ventilation, Environmental Research Letters, 18, https://doi.org/10.1088/1748-9326/acc346, 2023.

Liu, Y., Sun, D., Hu, X., Ye, X., Li, Y., Liu, S., Cao, K., Chai, M., Zhou, W., Zhang, J., Zhang, Y., Sun, W., and Jiao, L.: The Advanced Hyperspectral Imager: Aboard China's GaoFen-5 Satellite, IEEE Geoscience and Remote Sensing Magazine, 7, 23–32, 2019.

Loizzo, R., Guarini, R., Longo, F., Scopa, T., Formaro, R., Facchinetti, C., and Varacalli, G.: Prisma: The Italian Hyperspectral Mission, pp. 175–178, https://doi.org/10.1109/IGARSS.2018.8518512, 2018.

380 Lou, H., Zhang, J., Yang, S., Cai, M., Ren, X., Luo, Y., and Li, C.: Exploring the Relationships of Atmospheric Water Vapor Contents and Different Land Surfaces in a Complex Terrain Area by Using Doppler Radar, Atmosphere, 12, https://doi.org/10.3390/atmos12050528, 2021.

Manolakis, D., Lockwood, R., Cooley, T., and Jacobson, J.: Robust Matched Filters for Target Detection in Hyperspectral Imaging Data, in: 2007 IEEE International Conference on Acoustics, Speech and Signal Processing - ICASSP '07, vol. 1, pp. I–529–I–532,

385 https://doi.org/10.1109/ICASSP.2007.366733, 2007.

Masood, F., Ahmad, S., and Malik, A.: Role of Methanotrophs in Mitigating Global Warming, pp. 43–60, Springer Singapore, Singapore, https://doi.org/10.1007/978-981-33-4508-9_4, 2021.

Mayfield, E. N., Robinson, A. L., and Cohon, J. L.: System-wide and Superemitter Policy Options for the Abatement of Methane Emissions from the U.S. Natural Gas System, Environmental Science & Technology, 51, 4772–4780, https://doi.org/10.1021/acs.est.6b05052, pMID:

390 28195720, 2017.

Mieruch, S., Schröder, M., Noël, S., and Schulz, J.: Comparison of decadal global water vapor changes derived from independent satellite time series, Journal of Geophysical Research: Atmospheres, 119, 12,489–12,499, https://doi.org/https://doi.org/10.1002/2014JD021588, 2014.

Ming, T., Li, W., Yuan, Q., Davies, P., de Richter, R., Peng, C., Deng, Q., Yuan, Y., Caillol, S., and Zhou, N.: Perspectives on removal of

395 atmospheric methane, Advances in Applied Energy, 5, 100 085, https://doi.org/https://doi.org/10.1016/j.adapen.2022.100085, 2022.

Ocko, I. B., Sun, T., Shindell, D., Oppenheimer, M., Hristov, A. N., Pacala, S. W., Mauzerall, D. L., Xu, Y., and Hamburg, S. P.: Acting rapidly to deploy readily available methane mitigation measures by sector can immediately slow global warming, Environmental Research Letters, 16, 054 042, https://doi.org/10.1088/1748-9326/abf9c8, 2021.

Roger, J., Irakulis-Loitxate, I. Valverde, A., Gorroño, J., Chabrillat, S., Brell, M., and Guanter, L.: High-resolution methane mapping with
400   the EnMAP satellite imaging spectroscopy mission [Preprint], https://doi.org/https://doi.org/10.31223/X5M65Z, 2023.

Thompson, D. R., Leifer, I., Bovensmann, H., Eastwood, M., Fladeland, M., Frankenberg, C., Gerilowski, K., Green, R. O., Kratwurst, S.,
    Krings, T., Luna, B., and Thorpe, A. K.: Real-time remote detection and measurement for airborne imaging spectroscopy: a case study
    with methane, Atmospheric Measurement Techniques, 8, 4383–4397, https://doi.org/10.5194/amt-8-4383-2015, 2015.

Thompson, D. R., Thorpe, A. K., Frankenberg, C., Green, R. O., Duren, R., Guanter, L., Hollstein, A., Middleton, E., Ong, L., and Ungar,
405   S.: Space-based remote imaging spectroscopy of the Aliso Canyon CH4 superemitter, Geophysical Research Letters, 43, 6571–6578,
    https://doi.org/10.1002/2016GL069079, 2016.

UNEP: Global Methane Assessment: Benefits and Costs of Mitigating Methane Emissions, https://www.unep.org/resources/report/
    global-methane-assessment-benefits-and-costs-mitigating-methane-emissions, 2021.

Varon, D. J., Jacob, D. J., McKeever, J., Jervis, D., Durak, B. O. A., Xia, Y., and Huang, Y.: Quantifying methane point sources
410   from fine-scale satellite observations of atmospheric methane plumes, Atmospheric Measurement Techniques, 11, 5673–5686,
    https://doi.org/10.5194/amt-11-5673-2018, 2018.